

# Jamming prokaryotic cell-to-cell communications in a model biofilm†

Winston Timp,<sup>‡a</sup> Utkur Mirsaidov,<sup>‡b</sup> Paul Matsudaira<sup>a</sup> and Gregory Timp<sup>\*b</sup>

Received 17th June 2008, Accepted 13th November 2008

First published as an Advance Article on the web 11th December 2008

DOI: 10.1039/b810157d

We report on the physical parameters governing prokaryotic cell-to-cell signaling in a model biofilm. The model biofilm is comprised of bacteria that are genetically engineered to transmit and receive quorum-sensing (QS) signals. The model is formed using arrays of time-shared, holographic optical traps in conjunction with microfluidics to precisely position bacteria, and then encapsulated within a hydrogel that mimics the extracellular matrix. Using fluorescent protein reporters functionally linked to QS genes, we assay the intercellular signaling. We find that there isn't a single cell density for which QS-regulated genes are induced or repressed. On the contrary, cell-to-cell signaling is largely governed by diffusion, and is acutely sensitive to mass-transfer to the surroundings and the cell location. These observations are consistent with the view that QS-signals act simply as a probe measuring mixing, flow, or diffusion in the microenvironment of the cell.

## Introduction

Quorum sensing (QS) is a prime example of paracrine signaling in which a cell affects gene expression in a neighboring cell.<sup>1</sup> According to the classic QS hypothesis, bacteria communicate and count their numbers by producing, releasing, and detecting small, diffusible, signaling molecules called autoinducers (AI). Quorum-sensing has been implicated in the regulation of processes such as bioluminescence, swarming, swimming, and virulence.<sup>1–5</sup> But despite its appeal, the QS hypothesis may not be an accurate description of all these phenomena.<sup>6–8</sup>

To elucidate how cell-to-cell signaling works in bacteria, it is vital to control signal transmission between cells,<sup>7</sup> yet most of the experiments used to test QS are done in a shaken culture flask, where the signal accumulates to a threshold concentration along a growth curve. It is difficult to emulate the diffusion, mixing and flow of signals found *in vivo* using a flask. In particular, bacteria naturally co-exist in sessile communities called biofilms.<sup>9–12</sup> A biofilm is comprised of microcolonies of bacteria encapsulated in a hydrated matrix of polysaccharides, proteins and exopolymeric substances. The mass transport in a biofilm may exhibit gross deviations from Brownian diffusion—in some cases the diffusion coefficient is 50× smaller than in aqueous solutions<sup>13</sup>—and so the chemistry can vary drastically over a short (100 μm) distance and have a profound effect on signal transmission, production rate, and half-life.<sup>7</sup>

Here, we report on the physical parameters governing prokaryotic cell-to-cell signaling in a model biofilm. The model biofilm is comprised of bacteria that are genetically engineered to transmit and receive QS signals. The biofilm is formed using

arrays of time-shared, holographic optical traps in conjunction with microfluidics to precisely position bacteria, and then encapsulated within a hydrogel that mimics the extracellular matrix.<sup>14</sup> Using fluorescent protein reporters functionally linked to QS genes, we assay the intercellular signaling with microscopy. Contrary to the QS hypothesis, there does not seem to be a single cell density for which QS-regulated genes are induced or repressed. Instead, the “information” communicated by the AI concentration depends on the environmental conditions. Cell-to-cell signaling is largely governed by diffusion, and it is acutely sensitive to mass-transfer to the surroundings and the cell location. These observations are consistent with the view advocated by Redfield,<sup>8</sup> and others,<sup>6</sup> which posits that an AI acts simply as a probe measuring mixing, flow, or diffusion in the microenvironment of the cell.

## Results

We tested the physical parameters governing paracrine signaling between bacteria in a diffusion-limited microenvironment by tracking *lux* gene expression in a community formed by assembling specialized bacteria into microarrays in hydrogel. Two genes are involved in QS in *V. fischeri*: *luxI* which encodes an enzyme catalyzing production of N-3-oxo-hexanoyl-homoserine lactone (C6-HSL), the *V. fischeri* AI; and *luxR*, which encodes a C6-HSL-dependent transcriptional activator. We separated the *lux* genes into transmitter and receiver plasmids, as shown in Figs. 1(A) and (B) and then transformed *E. coli* with them.<sup>15</sup> This produced the signaling networks shown in Fig. 1(C). By using a *lac* promoter to regulate *luxI* expression in the transmitter cells as shown in Fig. 1(A), we can control the production of the C6-HSL AI by addition of isopropyl-β-D thiogalactopyranoside (IPTG).

Both bacteria use fluorescent proteins linked to the QS genes to report gene expression. The transmitter cells express mRFP1 when induced by IPTG, and the receiver cells express GFP-LVA when activated by C6-HSL. GFP-LVA has a *ssrA* tag on the C-terminus, with the final amino acids being leucine(L),

<sup>a</sup>Whitehead Institute, Massachusetts Institute of Technology, Cambridge, MA, 02139, USA. E-mail: timp0@alum.mit.edu; matsudaira@wi.mit.edu

<sup>b</sup>3041 Beckman Institute, University of Illinois at Urbana-Champaign, 405 North Mathews Avenue, Urbana, IL, 61801, USA. E-mail: gtimp@uiuc.edu; uzphoton@uiuc.edu; Fax: +217-244-6622; Tel: +217-244-9629

† Electronic supplementary information (ESI) available: Supplementary figures S1–S4. See DOI: 10.1039/b810157d

‡ Contributed equally to this work.

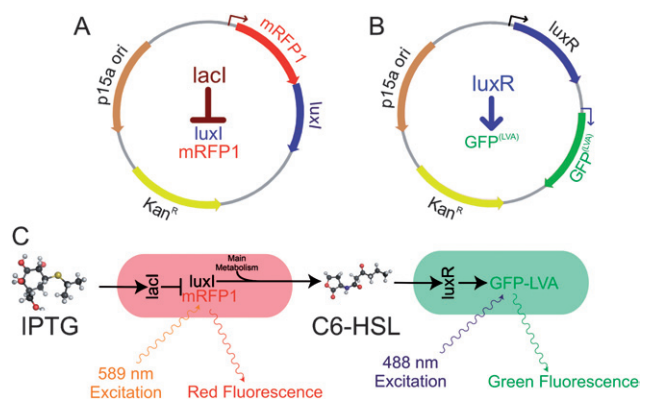


**Fig. 1** (A) Transmitter bacteria (4689 bp) produce *luxI* (C6-HSL producing enzyme) as well as mRFP1 under control of the *lac* operon induced with IPTG. (B) Receiver bacteria, (3739 bp) produce *luxR* (C6-HSL-binding protein) constitutively under the *luxP(L)* promoter. *LuxR* binds to C6-HSL, then dimerizes and binds to the *lux* operon, upregulating *luxP(R)* and downregulating *luxP(L)*. Upon receipt of C6-HSL, receivers produce GFP-LVA, a rapidly degradable form of GFP. (C) A simple model of paracrine based cell signalling similar to quorum sensing in bacteria, using the transmitter bacteria (red) to produce a chemical signal and the receiver bacteria (green) to detect this signal.

valine(V) and alanine(A), marking the GFP for degradation by the native protease ClpXP. This degradable variant shortens the half-life of GFP-LVA to  $\sim 40$  min, providing a means for measuring transient gene expression.<sup>16</sup>

Microarrays comprised of transmitter and/or receiver cells were formed in a photopolymerized hydrogel using optical tweezers in conjunction with a microfluidic to precisely assemble the cells, as illustrated schematically in Fig. 2(A). Multiple laminar fluid flows in the microfluidic device shown in Fig. 2(B) were employed to convey different cell types to an assembly area, where dynamically controlled optical traps were used to precisely position the different bacteria into an array, as described in detail elsewhere.<sup>17</sup> In brief, heterologous arrays of bacteria are assembled in the clear channel of the microfluidic at the location highlighted in Fig. 2(B) with optical tweezers (red beam in Fig. 2(A)) formed using two different diffractive elements: acousto-optical deflectors (AODs); and a spatial light modulator. Two dimensional  $2 \times 2$  microarrays were first assembled using the AODs, and then the SLM was used to introduce a slight divergence so that the pattern of traps would come to focus at a different point along the optical axis. The microarray is assembled one cell at a time in less than 6 min. While optical trapping can be used to create vast networks of cells resembling tissue,<sup>17</sup> the trapping beam still has to be held on the cells to maintain the array. So, once a microarray is assembled with tweezers, we fix the position of the cells permanently by exposing a photopolymerizable pre-polymer solution in the clear channel to  $\sim 1$  mW of UV light at  $\lambda = 360 \pm 20$  nm (blue beam in Fig. 2(A)) for  $\sim 3$  s to form a hydrogel. The inset to Fig. 2(A) is a confocal image showing a  $3 \times 2 \times 2$  microarray of *E. coli* assembled in hydrogel, imaged using a rhodamine dye. A magnified view of the same microarray is shown in Figs. 2(C) and (D). It is comprised of three two dimensional (2D)— $2 \times 2$  arrays of individual *E. coli* bacterium separated along the optical  $z$ -axis

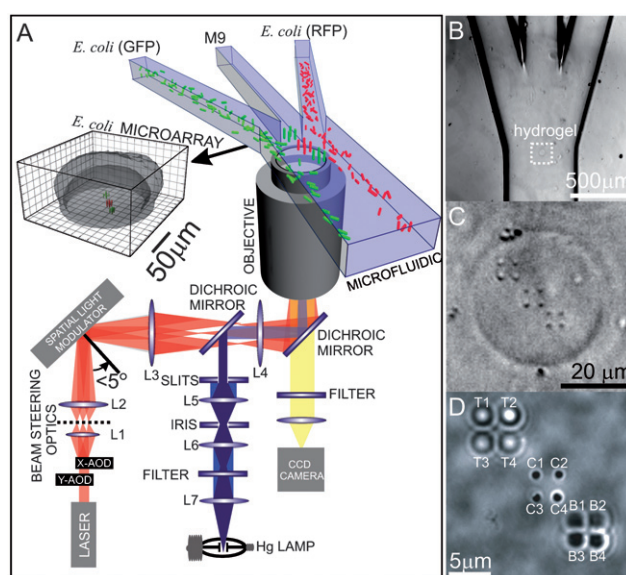


**Fig. 2** (A) Trap arrays (red) are formed using a high NA objective in a commercial optical microscope in conjunction with two AODs and an SLM to produce a time-multiplexed 3D array of optical traps. A typical hydrogel microstructure encapsulating a  $5 \times 5$  array of *E. coli* is shown in the inset to (D). The same microscope that is used to produce the cell traps is also used for viewing (via the yellow beam) and forming the hydrogel microstructure with a UV exposure (blue). The cells are conveyed to the assembly chamber using a microfluidic network like that shown in the transmission micrograph in (B). Multiple laminar fluid flows in the microfluidic network convey genetically engineered *E. coli* to an assembly area highlighted by the dashed square. The transmitter cell type flows in from the left, the receivers flow in from the right, while the center channel where the array is assembled has only clear solution. The gel spot is formed in the center channel, highlighted by the square and zoomed in (C). (D) A  $2 \times 2 \times 3$  3D microarray of *E. coli* which have been transformed into transmitters and receivers and positioned in hydrogel. The image is taken with the focus at  $z = 9 \mu\text{m}$  at  $t = 0$ , just prior to induction.

by  $9 \mu\text{m}$ , and offset in the  $x$ - $y$  plane by  $5 \mu\text{m}$ . The 3D nature of the array is indicated by the focus condition. The camera focal plane is coplanar with an array of transmitter cells located at  $z = 9 \mu\text{m}$  causing the bottom ( $z = 0 \mu\text{m}$ ) and top ( $z = 18 \mu\text{m}$ )  $2 \times 2$  arrays to be slightly out of focus.

We can manipulate the microenvironment of a cell within a microarray using the microfluidic network in which it is embedded to deliver ligands exogenously. For example, as illustrated in Fig. 3, we show that it is possible to induce gene expression in a microarray comprised of receivers *only*. GFP expression in a receiver array is affected solely by the concentration of C6-HSL. So for calibration, we first studied the receiver response to exogenously applied C6-HSL in the  $3 \times 3$  array shown in Fig. 3(A). The space-time dependence of the fluorescence is shown in Fig. 3(B). At  $t = 0$ , 10 nM of C6-HSL in M9 was broadcast into the microarray using a nearly static flow ( $0.03 \mu\text{L}/\text{min}$ ); green fluorescence is observed about 200 min later. At  $t = 420$  min the flow in the microfluidic is switched from 10 nM (C6-HSL) at  $0.03 \mu\text{L}/\text{min}$  to 0 nM at  $0.8 \mu\text{L}/\text{min}$ , and the fluorescence diminishes—nearly vanishing by 525 min. But when the 10 nM (C6-HSL) signal is re-established at 640 min, the fluorescence returns.

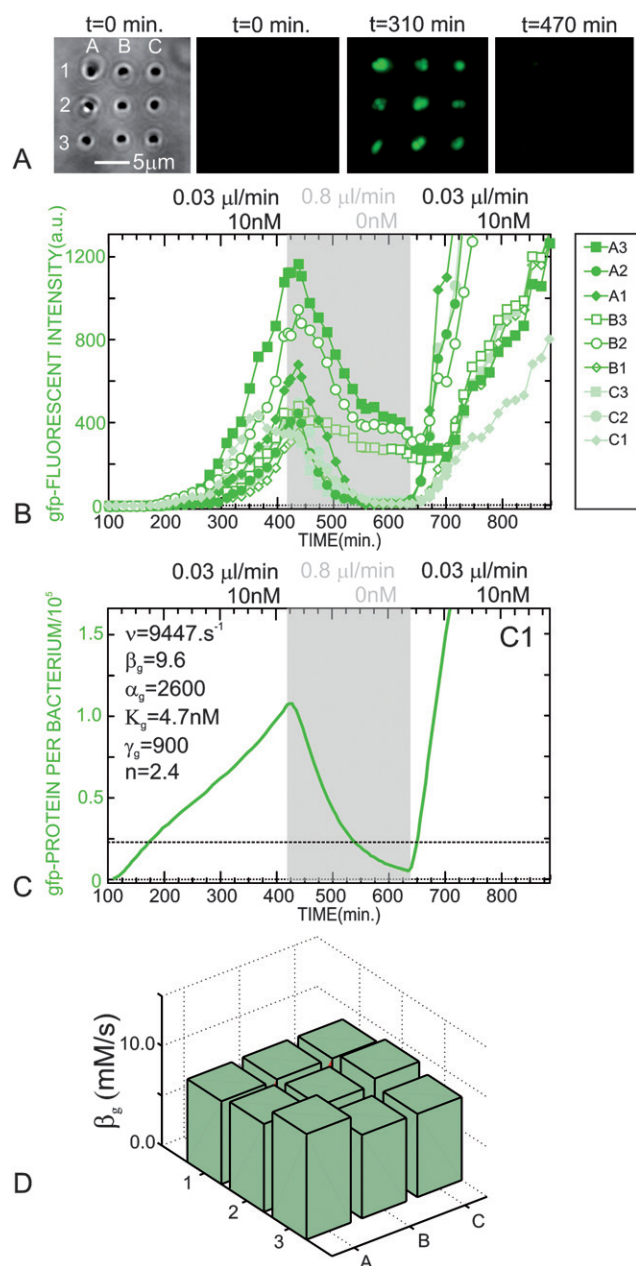


**Fig. 3** Gene expression in  $3 \times 3$  array of receivers induced exogenously using a microfluidic. (A) Transmission and fluorescent micrographs of a  $3 \times 3$  microarray of receiver bacteria fixed in hydrogel. At  $t = 0$ , 10 nM of C6-HSL in M9 is broadcast into the array in nearly stagnant flow (0.03  $\mu\text{L}/\text{min}$ ) using the micro fluidic, causing the cells to produce GFP-LVA. At 420 min, the concentration and flow condition is changed to 0 nM C6-HSL at a flow of 0.8  $\mu\text{L}/\text{min}$  and the green fluorescence diminishes. At 640 min the original concentration (10 nM of C6-HSL) and flow condition 0.03  $\mu\text{L}/\text{min}$  is re-established and the fluorescence returns. (B) Plots of the fluorescent intensity corresponding to A for individual cell/microcolonies comprising the array as a function of time. (C) A plot of the simulated fit to element C1 with the parameters shown in the inset. (D) A histogram showing the different values for maximal protein expression for individual bacteria/microcolonies, illustrating the noise giving rise to cell-cell variation.

By analyzing the spatial–temporal development of the fluorescence in microarrays, we can infer information about the elements affecting the dynamics of the fluorescent reporters in the microarrays. Eqn 1(a) and (b), *i.e.*

$$\frac{\partial[\text{GFP}_{\text{unox}}]}{\partial t} = \beta_g 2^{t/\nu_g} \frac{[\text{C6-HSL}]^n}{[\text{C6-HSL}]^n + K_g^n} - (\gamma_g + \alpha_g)[\text{GFP}_{\text{unox}}] \quad (1a)$$

$$\frac{\partial[\text{GFP}_{\text{ox}}]}{\partial t} = \gamma_g[\text{GFP}_{\text{unox}}] - \alpha_g[\text{GFP}_{\text{ox}}] \quad (1b)$$

capture the rate of change of unoxidized  $[\text{GFP}_{\text{unox}}]$  and oxidized  $[\text{GFP}_{\text{ox}}]$  concentrations of GFP-LVA. GFP-LVA protein concentration is a balance between production, at a rate given by the product of the Hill function associated with the C6-HSL input,  $\beta_g$ , oxidation which occurs at a rate  $\gamma_g$ , and degradation of GFP through proteolytic digestion at a rate  $\alpha_g$ . To account for bacterial reproduction, we allow  $\beta$  to vary with time according to  $\beta_g 2^{t/\nu}$ , where  $\nu$  is the rate constant for doubling. Using eqn (1) we simulated and fit the GFP-LVA expression measured by the fluorescence data to extract parameters that described GFP production and degradation, and the C6-HSL concentration profiles within the array (see Methods). We assumed that the time scale needed for C6-HSL to diffuse into the hydrogel is much faster than the response time of the cell, allowing us to represent the C6-HSL concentration by a smoothed step function between different C6-HSL levels. This assumption was justified by measurements of fluorescein diffusion (a similar size molecule) in a hydrogel spot (see ESI†). Fig. 3(C) shows a typical example of a fit to an element of the array. Using this fit, we characterized the receiver bacteria, extracting the following parameters:  $n = 2.4$ ,  $\beta_g \sim 9$  molecules/s,  $\gamma_g = \ln(2)/900 \text{ s}^{-1}$ ,  $\alpha_g = \ln(2)/2600 \text{ s}^{-1}$ , and  $\nu \sim 12000 \text{ s}$  with  $K_g = 4.7 \text{ nM}$ .

The strength of the green fluorescent response also depends on the idiosyncrasies of the cells in the array.<sup>18,19</sup> The plasmid copy number, the spatial distribution, and the fluctuating reactivity of biologically relevant molecules in each cell give rise to random variations in the outcome as evident from Fig. 3(B). Thus, cell dynamics are affected not only by the microenvironment defined by multiple cell types and social context, but also by the regulation circuits and the noise associated with stochastic variations. We can infer information about all of these elements affecting the dynamics through simulation of the individual responses. For example, Fig. 3(D) is a histogram showing a sample of one outcome: the maximal expression level of the promoter given by  $\beta_g$ . (In this estimate for  $\beta$  we accounted for the observation that the bacteria have multiplied due to the long duration of the experiment. The doubling time in M9 is about 2.5 hours and we are flowing M9 past the array at a rate of 0.2  $\mu\text{L}/\text{min}$ , which encourages the growth of microcolonies, so we counted the number of cells in each colony.) The microcolonies show a large difference in their  $\beta$  values illustrating the extrinsic noise causing cell–cell variation: *i.e.*  $\beta_{g0} = 8.6 \pm 0.7$  molecules/s, which we attribute to differences in the initial plasmid copy number (that is  $\sim 15$ ),<sup>20</sup> the metabolic level of the individual cells, and asynchrony of the cell cycle.

By controlling the mass transport to the fluid surrounding the hydrogel and the distances between cells, it is possible to manipulate communications between transmitters and receivers within the

same array mediated by C6-HSL. To demonstrate this, we constructed a  $3 \times 2 \times 2$  array of bacteria with the central ( $z = 9 \mu\text{m}$ )  $2 \times 2$  array consisting of transmitter bacteria and the top and bottom ( $z = 18, 0 \mu\text{m}$ )  $2 \times 2$  arrays consisting of receiver bacteria. The space–time development of fluorescence observed in the transmitter and receiver arrays is shown in Fig. 4(A–C), while Fig. 4(D) quantitatively tracks fluorescent intensity for each element of the microarray. Starting at  $t = 0$ , we used the microfluidic to deliver 2 mM of IPTG in M9 media at a  $0.03 \mu\text{L}/\text{min}$  flow rate in order to induce the *lac* operon in the transmitters. This flow rate corresponds to a measured fluid velocity of about  $<2 \mu\text{m}/\text{s}$  so that the dominant transport mechanism in the vicinity of the hydrogel is diffusion (with Péclet number  $<1$ , see ESI†). About 250 min later, red fluorescence can be observed above the background in Fig. 4(B), and increases continuously after that point indicating the production of luxI and therefore C6-HSL. When the C6-HSL concentration in the hydrogel exceeds threshold near  $t = 600$  min, the receivers produce sufficient GFP-LVA to observe fluorescence above background. By this time the individual bacteria in the array have replicated, forming micro-colonies.

We used the flow rate through the microfluidic network to modulate the signal concentration in the hydrogel to affect cell communications. Fig. 4(D) shows that both the red and green fluorescence continue to increase in intensity in the interval  $600 \text{ min} < t < 675 \text{ min}$  until the flow is abruptly changed at  $t = 675 \text{ min}$  from  $0.03 \mu\text{L}/\text{min}$  to  $0.8 \mu\text{L}/\text{min}$  (increasing the fluid velocity to  $\sim 30 \mu\text{m}/\text{s}$  at  $z \sim 20 \mu\text{m}$ ). The increase in flow velocity changes the mass transport characteristics of the system ( $Pe > 1$ ), diluting the concentration of the C6-HSL in the hydrogel. The apparent drop of C6-HSL below threshold reduces GFP-LVA production, and subsequently proteolytic digestion diminishes the intensity of green fluorescence observed after  $t = 675 \text{ min}$ . Eventually, near  $t = 775 \text{ min}$ , green fluorescence is practically extinguished in both receiver arrays without a decrease in the number of bacteria. In this short time interval between 675 and 775 min the cell density doesn't change appreciably, yet the QS-regulated genes, which are expressed  $<675 \text{ min}$ , are evidently completely repressed based on the fluorescence. However, when the near static flow condition,  $0.03 \mu\text{L}/\text{min}$ , is re-established at  $t > 750 \text{ min}$ , the green fluorescence returns accordingly.

To extract parameters that describe mRFP1, luxI as well as GFP-LVA production and degradation, and the IPTG and C6-HSL concentration profiles within the array, we simulated the spatial–temporal dependence of the fluorescence data using the simple mass-action kinetics for the protein production described above, but this time accounting for the protein dynamics for transmitters as well as receivers. Eqn 2(a)–(c), *i.e.*

$$\frac{\partial[\text{RFP}_{\text{unox}}]}{\partial t} = \beta_r 2^{t/\nu_r} \frac{[\text{IPTG}]^n}{[\text{IPTG}]^n + K_r^n} - \gamma_r [\text{RFP}_{\text{unox}}] \quad (2a)$$

$$\frac{\partial[\text{RFP}_{\text{ox}}]}{\partial t} = \gamma_r [\text{RFP}_{\text{unox}}] \quad (2b)$$

$$\frac{\partial[\text{luxI}]}{\partial t} = \beta_r 2^{t/\nu_r} \frac{[\text{IPTG}]^n}{[\text{IPTG}]^n + K_r^n} \quad (2c)$$

capture the rate of change of unoxidized mRFP1, oxidized (or fluorescent mRFP1), and luxI. These equations were coupled to

a finite element model for convection–diffusion transport, to determine the resulting concentration profile of the C6-HSL. The concentration profile for C6-HSL was then used with eqn 1(a) and (b) to describe the concentration of GFP-LVA.

Relying on these relationships and the constraints on the coefficients obtained from simulations of independent measurements like those shown in Fig. 3, we simulated the fluorescence observed in the arrays and extracted parameters that described mRFP1 and GFP-LVA protein production and degradation, as well as the concentration profiles within the array of Fig. 4. To accomplish this, we first fit the transmitter behaviour to eqn (2), assuming that IPTG reaches a steady-state concentration rapidly. We extracted the following parameters for the transmitter cells:  $n = 3$ ,  $\beta_r = 20 \text{ molecules}/\text{s}$ ,  $\gamma_r = \ln(2)/720 \text{ s}^{-1}$ ,  $\alpha_r = 0$ ,  $\nu = 15000 \text{ s}$ , and  $K_r = 50 \mu\text{M}$ . We then used the results of this fit to extract a value for luxI concentration, which we assumed to be stoichiometric with the mRFP1 concentration. This concentration is coupled into a mass transport finite element model to determine the evolution of concentration of C6-HSL in the hydrogel over time. The C6-HSL concentration detected by the receiver bacteria is then used to calculate the amount of GFP-LVA produced, using the previously calibrated parameters. To fit the data, the least-square difference between the theoretical GFP-LVA concentration and observed green fluorescence is minimized, while the diffusion coefficient, rate of C6-HSL production per molecule of luxI and values for  $\beta_g$  and  $\nu_g$  of the individual bacteria are allowed to vary. This allows for a full description of our observed data *via* the simulation. Fig. 4(E) shows solid red and green lines that represent the mRFP1 and GFP-LVA production, while Figs. 4(F–H) show the concentration profile of C6-HSL. Provided that the threshold for observing the green and red fluorescence is  $\sim 2 \times 10^4 \text{ molecules per bacterium}$ , the simulations in Fig. 4(E) resemble the observed fluorescence dynamics in response to changes in the flow. We find a large difference in the maximal expression level of the promoter as given by  $\beta$ . Matching the simulation to the data of Fig. 4(D), the microcolonies show a range of  $\beta$  values  $\beta_{r0} = 20.1 \pm 8.2 \text{ molecules}/\text{s}$  and  $\beta_{g0} = 6.36 \pm 1.1 \text{ molecules}/\text{s}$ , illustrating the stochastic nature of protein production. We attribute this to differences in the initial plasmid copy number ( $\sim 15$ ), the individual cell metabolism, and asynchronous cell cycle.

Complementary to Fig. 4, the data of Fig. 5 indicates that the receiver array's response is affected, not only by the flow, but also by the relative position of the elements to the transmitter array. The data was obtained from a microarray with the middle and top arrays at  $z = 9 \mu\text{m}$  and  $z = 18 \mu\text{m}$  comprised of receivers, while the bottom array at  $z = 0 \mu\text{m}$  is comprised of transmitters. The space–time development of the fluorescence is shown in Fig. 5(A–C), while Fig. 5(D) quantitatively tracks the intensity for each (live) element of the receiver arrays, normalized to the maximum for each element. Starting at  $t = 0$ , we used the microfluidic to deliver 2 mM of IPTG in M9 minimal media at a  $0.03 \mu\text{L}/\text{min}$  flow rate to induce the transmitters. At  $t = 300 \text{ min}$  later, red fluorescence can be observed above the background, increasing continuously indicating production of C6-HSL. The C6-HSL concentration eventually exceeds threshold causing the receivers to produce GFP-LVA. Under the low flow condition, the receiver bacteria apparently turn on simultaneously, similar to the behavior shown in Fig. 4. But an increase in the flow rate

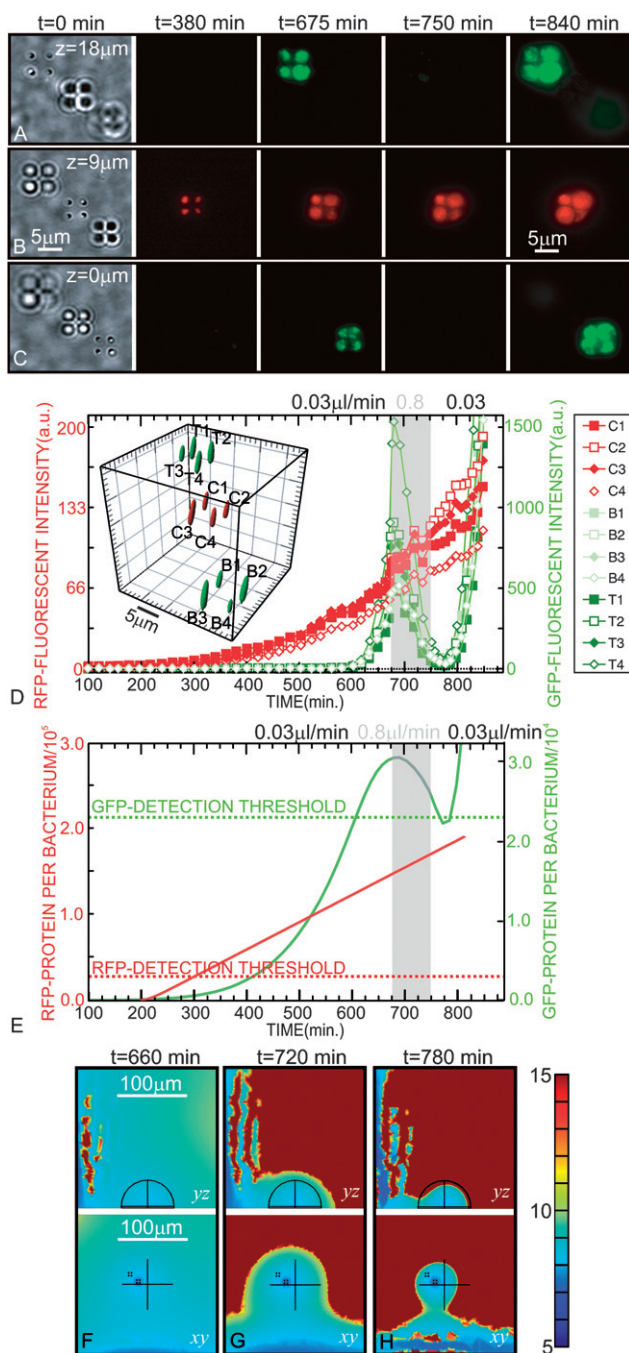


**Fig. 4** Gene expression in a  $2 \times 2 \times 3$  array with a transmitter subarray between two receiver arrays. (A), (B), and (C) are transmission and fluorescent micrographs with the focus at  $z = 18 \mu\text{m}$ ,  $9 \mu\text{m}$  and  $18 \mu\text{m}$  respectively. A  $2 \times 2$  array of transmitter cells is located in the center plane at  $z = 9 \mu\text{m}$ , while  $2 \times 2$  arrays of receivers are located at  $z = 0 \mu\text{m}$  and  $18 \mu\text{m}$ . The first images in (A–C) are transmission micrographs taken at  $t = 0$ , just prior to induction. When  $2 \text{ mM}$  IPTG in M9 media is broadcast to the array at  $0.03 \mu\text{l}/\text{min}$  flow, the transmitters detect the inducer in their microenvironment above threshold and upregulate production of mRFP1 (red fluorescence) along with LuxI, generating C6-HSL. At  $t > 250 \text{ min}$ , red fluorescence rises to a detectable level, as illustrated by the fluorescence micrographs. When the concentration of C6-HSL is sufficient, near  $t = 600 \text{ min}$ , the receivers upregulate green fluorescent protein production, allowing detectable accumulation. At  $675 \text{ min}$  the flow in the microfluidic is increased from  $0.03 \mu\text{l}/\text{min}$  to  $0.8 \mu\text{l}/\text{min}$

to  $0.8 \mu\text{l}/\text{min}$  at  $t = 970 \text{ min}$  sweeps the C6-HSL out of the hydrogel. A gradient is formed with the middle and top arrays detecting different local concentration of C6-HSL. Consequently, the balance between protein production and proteolytic degradation shifts, causing a decrease in the concentration of GFP-LVA. The receiver cells in elements T1, T2 and T3 in the top ( $z = 18 \mu\text{m}$ ) array lose fluorescence rapidly, as they have a lower local concentration of C6-HSL, due to their relative proximity to the high Péclet number external flow. The fluorescence declines at a slower rate in elements C1–C4, as the local concentration of C6-HSL remains higher.

## Discussion

*In-situ* observation of biofilm structure found in nature reveals sessile bacteria growing in heterogeneous matrix-enclosed microcolonies.<sup>21,22</sup> In a flowing environment, some biofilms exhibit an architecture consisting of specialized cells with AIs playing a role in the differentiation process.<sup>23</sup> An analysis of gene expression within a microcolony has shown that AIs are maximally expressed in cells located in the substratum in a biofilm and that expression decreases with increasing height in the mushroom-like microstructure.<sup>24</sup> This complex architecture is an indication that biofilm development is not simple and uniform, but rather complex and differentiated.<sup>10</sup>

A popular method for studying biofilms is based on passing a bacterial suspension through a flow-cell to which cells adhere and grow into a biofilm.<sup>25,26</sup> This method enables reproducible film formation, but there is no control of the architecture—only single species biofilms have been studied so far. On the contrary, polymicrobial biofilm infections are prevalent in clinical environments,<sup>27,28</sup> and communalism in them can spawn antibiotic resistance<sup>29</sup>—so, there is a need for relevant models. And there is also a need for relevant testing protocols. The inability to assess the chemical gradients or gradients of gene expression presents yet another challenge to current biofilm research. Almost every study to date uses *DNA* microarray or proteomic analysis of a biofilm population to take an *average* of the expression profile over the entire population even though biofilms are heterogeneous and differentiated.<sup>26</sup>

and green fluorescence diminishes subsequently, as illustrated by the figures taken at  $t = 750 \text{ min}$ . When the flow is restored, green fluorescence returns as illustrated by the fluorescence micrographs taken at  $t = 840 \text{ min}$ . (D) Plots of the fluorescent intensity corresponding to (A–C) for individual cells/microcolonies comprising the array as a function of time. The inset in D is a false-color perspective iso-surface, reconstructed from volumetric data obtained from a series of confocal images, showing a  $2 \times 2 \times 3$  three-dimensional array of *E. coli*. The inset identifies the individuals in the array. (E) Simulations of the fluorescent intensities. The red line represents a simulation of the mRFP protein concentration, resulting from eqn (1) in the text. The green line represents a simulation of the GFP-LVA protein concentration, derived from eqn (2) and a convection-diffusion simulation of the C6-HSL concentration with respect to time. (F–H) Contour plots of the C6-HSL concentration obtained from 3D simulations based on eqn. (1) and (2), taken from a  $yz$  cross-section taken at  $x = 0$  (top) and  $xy$  cross-section taken at  $z = 9 \mu\text{m}$  (center) at  $t = 675 \text{ min}$ , in near stagnant conditions with  $0.03 \mu\text{l}/\text{min}$ ;  $t = 750 \text{ min}$  after the change in flow to  $0.8 \mu\text{l}/\text{min}$ ; and  $t = 825 \text{ min}$  after re-establishing the flow at  $0.03 \mu\text{l}/\text{min}$ . The C6-HSL gradient is especially steep during high flow conditions  $0.8 \mu\text{l}/\text{min}$  and even after the nearly stagnant condition is re-established  $0.03 \mu\text{l}/\text{min}$ .

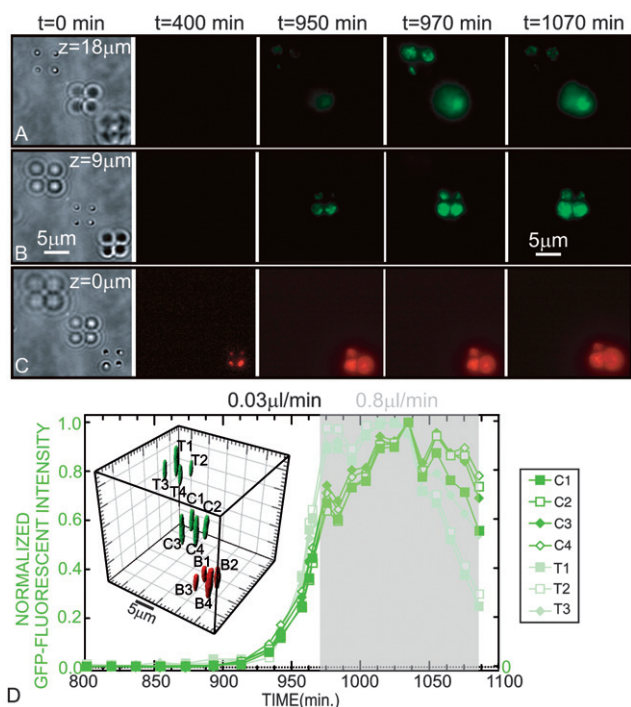


**Fig. 5** Gene expression in  $2 \times 2 \times 3$  array with a transmitter subarray below two receiver arrays. (A–C) Transmission and fluorescent micrographs with the focus at  $z = 18 \mu\text{m}$ ,  $9 \mu\text{m}$  and  $0 \mu\text{m}$  respectively. The first images in (A–C) are transmission micrographs taken at  $t = 0$ , just prior to induction. A  $2 \times 2$  array of transmitters is located in the center plane at  $z = 0 \mu\text{m}$ , while  $2 \times 2$  arrays of receivers are located at  $z = 9 \mu\text{m}$  and  $18 \mu\text{m}$ . When  $2 \text{ mM}$  IPTG in M9 media is broadcast to the array at  $0.03 \mu\text{L}/\text{min}$  flow, the transmitters detect the inducer in their microenvironment above threshold and begin to produce mRFP1 (red fluorescence) along with luxI, generating C6-HSL. When  $t > 250$  min, red fluorescence rises to a detectable level, as illustrated by the fluorescence micrographs shown in C. When the concentration of C6-HSL is sufficient at  $t = 950$  min, the receivers produce detectable amounts of green fluorescent protein as illustrated in A and B. At 970 min the flow in the microfluidic is increased from  $0.03 \mu\text{L}/\text{min}$  to  $0.8 \mu\text{L}/\text{min}$  and the green fluorescence in the top array is diminished while the fluorescence in the center array persists, as illustrated in A and B. (D) The history of the fluorescent intensity corresponding to (A–C) for individual cells/microcolonies, normalized to the maximum expression of each element, the inset in D is a false-color perspective iso-surface, reconstructed from volumetric data obtained from a series of confocal images, showing a  $2 \times 2 \times 3$  three-dimensional array of *E. coli*. The inset identifies the individuals in the array. (Cells B2 and T4 were unresponsive.)

To illuminate the role signaling plays in differentiation in a biofilm, we have created a biofilm model that mimics some of the essential features found in nature. The model is formed from bacterial microarrays assembled in hydrogel using optical traps in conjunction with microfluidics to precisely position the cells. This model has several advantages for studying cell-to-cell communications and controlling signal transmission between cells, not all of which are exploited in this report. First of all, this model allows for single cell analyses of signaling and yet still captures the essential complexity found in a biofilm. The architecture and constitution of the biofilm can be controlled using laser-guided assembly with a step-and-repeat methodology.<sup>17</sup>

Moreover, the rate of signal production, which depends on the genetics, and the relative position of the cells can be easily manipulated. The signal half-life may be affected either through chemistry using pH, growth substrate, or chemicals delivered exogenously to the array or by proteins produced endogenously by cells within the array. The diffusivity of the signal could also be controlled by manipulating the molecular weight, constituency, and gelling conditions of the hydrogel to affect the porosity and polarity of the scaffold. And finally, signal transmission between cells can be manipulated through mass-transfer using microfluidics to control the hydrodynamics of the overlying fluid.

In this study, we altered the mass-transfer characteristics of the bacterial autoinducer using microfluidics to control the hydrodynamics of the overlying fluid. We also controlled the spatial positioning of the microarray using optical trapping to place individual bacterial cells in heterotypic arrays. In order to determine the effect of the cells on each other, to control their microenvironment, the position of the different cells relative to each other has to be controlled. The shape and strength of the gradient will be largely defined by this positioning.

The homotypic microarray of Fig. 3 illustrates unequivocally the necessity for single-cell analysis. Bacteria, which are ostensibly genetically identical, all show expression in response to the AI delivered exogenously, but the response is quantitatively different. These differences would be obscured in a bulk measurement.

The heterotypic microarrays of transmitter and receiver cells shows the superiority of this model to other culture platforms such as multi-well plates where the air-liquid interface induces convective flow that continuously mixes the fluid and disrupts accumulation.<sup>30</sup> As transmitter cells of Fig. 4 and 5 generated C6-HSL, the AI diffused outward through the hydrogel, forming a gradient with respect to the surrounding bulk solution. The Damköhler number, a ratio of reaction speed to diffusion, tends towards zero in the microarray because protein production is much slower than C6-HSL diffusion. So, the concentration gradient is quasi-steady state, re-stabilizing rapidly in response to a change in the rate of production by the transmitters. As the C6-HSL production increases, the threshold concentration front moves slowly outward from the transmitters. Once the receivers bind enough C6-HSL to produce protein, the signal is not immediately apparent. There is a time-delay associated with production and maturation of GFP-LVA, that is captured by eqn (1) and the parameters used to fit the data of Fig. 3, as well as a need for sufficient fluorescent protein build up for CCD detection.

When the flow in the microfluidic is switched to  $0.8 \mu\text{L}/\text{min}$ , the microenvironment of the cells is dramatically altered. In order to demonstrate the different mass transport mechanisms under different flow conditions, we calculated the Péclet number along the  $z$ -axis centered on the hydrogel spot. The Péclet number is defined as the dimensionless ratio given by  $UL/D$ , where  $U$  is the flow velocity,  $L$  is the characteristic length, and  $D$  the diffusion coefficient. As shown in Fig S4 in the ESI, for the low flow condition ( $0.03 \mu\text{L}/\text{min}$ ),  $Pe < 1$ , indicating that in this regime, diffusion is the dominant mechanism of transport. So, the C6-HSL continues to diffuse outward through the microfluidic space, accumulating in and around the hydrogel spot. With the higher flow condition, C6-HSL transport is more

complicated, being dominated by convective transport in the center of the channel ( $Pe \sim 10$ ), and by diffusive transport in the stagnant layer near the hydrogel.

Our analysis reveals <50% change in the GFP-LVA concentration due to the switch in flow to 0.8  $\mu\text{L}/\text{min}$  for the transmitter–receiver array of Fig. 4. When the flow is switched, there is a large difference in the C6-HSL concentration profile present in and around the hydrogel spot, as illustrated by Fig. 4(F)–(H). For the nearly static flow condition, diffusion is the dominant transport mechanism, and C6-HSL builds up to a relatively uniform concentration in the hydrogel vicinity. In contrast, with the fast flow in the overlayer, there are regions where convective flow dominates driving the concentration down in the center of the microfluidic, where the parabolic flow profile provides the highest Péclet number ( $Pe \sim 10$ ). Diffusion then acts in and near the hydrogel spot to set up a gradient between the transmitters and the flow.

Thus, by modulating the flow in the overlayer, the local concentration of the signal in a microarray can be drastically altered, affecting gene expression. For high rates of flow, the green receiver fluorescence is nearly quenched; but, after the static flow condition is re-established, the fluorescence is revived within 50 min. This time scale is much shorter than the observed doubling time of the bacteria (15 000 s = 4.2 h) in minimal media in hydrogel. Consequently, the density of the bacteria does not change in this time interval.

By inference, the change in fluorescence observed in Fig. 4(D) with the changing flow conditions indicate that there isn't a single cell density for which QS-regulated genes are induced or repressed. Contrary to the QS hypothesis, the “information” communicated by the AI concentration likely depends on the environmental conditions, the density, the distribution, and type of cells producing signals. These observations are consistent with an alternative view advocated by Redfield,<sup>8</sup> which posits that AI acts simply as a probe measuring mixing, flow, or diffusion in the microenvironment of the cell. *This diffusion-sensing hypothesis is profoundly different from QS.*<sup>6,8</sup> According to Redfield, the AI doesn't really measure cell density or social activity at all, but rather it measures the mass-transfer in the environment of an *autonomous* bacterium, which eventually triggers behavior that benefits itself alone. The apparent synchronization in the response of a population is only a side effect of bacteria sensing their environment.

Since gene expression controls phenotype, signaling could produce phenotypes that depend on the flow and their location within the array. It is known that biofilms formed in a flowing environment exhibit an architecture consisting of specialized cells.<sup>23</sup> Our observations support the hypothesis that signaling plays a role in the differentiation process. If variations in gene expression result in the development of phenotypes that protect the film from attack, then these observations also lend themselves to explanations for the extraordinary resistance of biofilms to antimicrobial agents. Finally, these observations indicate the important role that mass transport plays in soluble factor signaling, in general. If the cells are at the top of an epithelial layer, or near a blood vessel, the soluble factors they are exposed to and the gradient of signal they see will be much different than cells embedded deep within tissue. An alteration of the extracellular matrix to alter the transport properties around cells may

alter their gene expression patterns and subsequent behavior dramatically.

## Materials and methods

### Strains, plasmids and genes

*E. coli* (*DH5 $\alpha$* ) was transformed with transmitter (4689 bp) and receiver (3739 bp) plasmids to express the *luxR* gene of *Vibrio fischeri*, following Weiss *et al.*<sup>15</sup> The transformed bacteria were grown on shakers at 37 °C in M9-Glycerol minimal media consisting of: 0.2% (v/v) glycerol, 42 mM  $\text{Na}_2\text{HPO}_4$ , 22 mM  $\text{KH}_2\text{PO}_4$ , 19 mM  $\text{NH}_4\text{Cl}$ , 9 mM NaCl, 1 mM  $\text{MgSO}_4$ , 100  $\mu\text{M}$   $\text{CaCl}_2$ , 200  $\mu\text{M}$  thiamine hydrochloride, and 0.2% (w/v) caseamino acids. 100  $\mu\text{g}/\text{mL}$  kanamycin was used as a selection marker.

Transmitter bacteria express *luxI* upon induction with IPTG, which subsequently catalyzes the formation of C6-HSL. C6-HSL then diffuses outward through the cell membrane. The receiver *E. coli* are sensitive to this signal, and respond by initiating gene expression through the regulating protein luxR. The receiver plasmid consists of the *luxP(L)* promoter controlling luxR production and the *luxP(R)* promoter controlling GFP-LVA production.<sup>16</sup> LuxP(L) acts natively as a weak constitutive promoter and is down-regulated in the presence of luxR–C6–HSL complex. On the other hand, *luxP(R)* has only a low level basal expression, and is strongly up-regulated in the presence of luxR–C6–HSL. When the concentration of the C6-HSL exceeds a threshold, the dimerized luxR–C6–HSL complex induces expression of a degradable variant of green fluorescent protein, GFP-LVA, through binding to the *luxP* promoter.

### Threshold measurements for gene expression

The threshold IPTG concentration for induction in the transmitters and C6-HSL concentration for induction in the receivers was determined by measuring fluorescence of bacteria taken from log-phase culture ( $\text{OD}_{600} = 0.1 \pm 0.02$  at  $T = 30$  °C.) The transformed bacteria were grown in culture in M9-Glycerol minimal media using kanamycin as a selection marker as described above.

Fluorescence data was collected using a Tecan Safire 96-well fluorescent plate reader. A 100  $\mu\text{L}$  volume of bacteria was seeded into each well of a 96-well plate, with each row derived from the same culture. A serial dilution of either IPTG or C6-HSL (depending on the bacteria being measured) was carried out across the plate, allowing the concentration to vary over several orders of magnitude. The plate was then placed into the temperature controlled plate reader, and measurements were taken every 15 min of  $\text{OD}_{600}$ , GFP fluorescence (488/507 nm), and mRFP1 fluorescence (587/610 nm).

After 6 h, the experiment was stopped, and the data collected. Using the end-point fluorescence from all of the wells, a curve showing concentration relative to fluorescence per well was produced as shown in Figure S1.† A simple Hill function was fit to the data to extract values for  $K$ , the threshold inducer concentration, and  $n$ . A threshold of 38  $\mu\text{M}$  IPTG with an  $n$  value of 2.1 was found for the transmitter cells, and a threshold of 4.7 nM C6-HSL with an  $n$  value of 2.5 for the receiver cells.

## Microfluidic devices

We used multiple laminar fluid flows in a microfluidic device to convey cells to an assembly area. The microfluidic device consisted of a three channel Y-junction similar to that shown in Fig. 2(B). The three entry-channels, which are 200  $\mu\text{m}$  wide, merged with an angle of 15° between neighboring channels into a single 600  $\mu\text{m}$  wide exit-channel. All the channels were 600  $\mu\text{m}$  in height. The microfluidic device was formed from poly-(dimethylsiloxane) (PDMS) using a mold-casting technique. The master mold, generated through off-site stereolithography based on a CAD file we designed (FineLine Prototyping), is made of a DSM Somos ProtoTherm 12120, a strong, high temperature tolerant plastic. To detach the PDMS without tearing the device, the mold is coated with a fluoropolymer, tridecafluor-1,1,2,2,(tetrahydrooctyl)-1-trichlorosilane, using vapor deposition in a vacuum oven at 75 °C and 20" Hg vacuum for 2 h. The PDMS silicone polymer used to create the chips is commercially available as Sylgard 184 (Dow Corning), a two part polymer mix. The two parts were mixed thoroughly at a 1 : 5 ratio of curing agent to base. The mixture was then degassed at house vacuum for 30 min. This mixture was poured into the master mold, and then cured at 75 °C for ~2 h. After cooling, the plastic, which has hardened to a rubber-like consistency, was peeled away from the mold, yielding a piece of silicone with the inverse pattern of the master mold.

The microfluidic channels were connected to external pressure and fluid reservoirs through a hole punched in the silicone chip at the input and output ports using a blunt syringe needle. Though PDMS is transparent our microfluidic chip is thick (>1000  $\mu\text{m}$ ) and light scattering through it prevents optical access through the top. Accordingly, to provide optical access we sealed the bottom of the PDMS using a piece of #1 cover glass. To tightly bind the PDMS microfluidic to the coverslip, a covalent bond between the PDMS and glass is formed using an oxygen plasma in a Harrick plasma cleaner (PDS-32G). The oxygen plasma generates silanol (Si–OH) groups on the surface of PDMS, which react with silanol groups on the glass surface to form a Si–O–Si bond. The plasma was monitored to ensure a bright, purplish color, and left on for 45 s. Finally, the PDMS chip was gripped by the sides, and placed in contact with the coverslip, and a uniform pressure was applied for 10 s to form the bond.

To enhance hydrogel adhesion and prevent bacterial adhesion, we treated the internal surfaces of the microfluidic device using a methacrylate silane treatment, which will crosslink with the hydrogel.<sup>31,32</sup> A 2% (v/v) solution of 3-(trimethoxysilyl)propyl methacrylate was made in 10 mL of 95% ethanol. The solution was adjusted to a pH of 5 using 50  $\mu\text{L}$  of glacial acetic acid. 500  $\mu\text{L}$  of this solution was pushed through the microfluidic chip using a 1 mL syringe, and incubated for 5 min at room temperature. The chip is then flushed out with 5 mL of deionized water. Finally, the chip is placed in an oven overnight at 85 °C.

## Cell microarray construction

1 mL samples of bacteria grown in M9 overnight at 25 °C were centrifuged 3 times for 5 min at 800 g. Between each spin cycle the supernatant was aspirated, and the bacterial pellet resuspended in 1 mL of M9-Glycerol media. Finally, a pre-polymer

mixture comprised of 3.4 kDa MW PEGDA (Laysan Bio) dissolved at 5% (w/v) in M9-Glycerol along with photoinitiator, 2-hydroxy-2-methyl-propiophenone at a concentration of 0.2% (v/v) was vigorously vortexed for 1 min, degassed for >5 min, and then combined with the cell suspension to create the desired concentration of PEGDA immediately before injection into the microfluidic.

## Optical tweezers

The microarrays are assembled in the microfluidic with optical tweezers produced at a wavelength  $\lambda = 900$  nm from a tunable CW Ti:sapphire laser (Spectra Physics) pumped at 532 nm by a 10W Nd:YVO<sub>4</sub> diode-pumped solid state laser (Spectra Physics), and a Zeiss Achroplan 100 $\times$  oil immersion objective (1.3 NA) held in an inverted optical microscope (Zeiss Axiovert 200M). As illustrated schematically in Fig. 2(A), multiple time-multiplexed traps were generated in three-dimensions by using a combination of AODs (AA-Optoelectronic) and an SLM (Boulder Nonlinear Systems), which were each optimized for maximum diffraction efficiency at the wavelength of interest. The laser beam is deflected transverse to the direction of propagation using two orthogonally-mounted AODs; giving independent control of the *x*- and *y*-positions of a trap, allowing for the creation of a 2D network of time-shared traps. The SLM was used as a Fresnel lens to offset the array along the optical axis. This electrically addressed nematic liquid crystal device acts as a 256 level kinoform in the optical path. 512 by 512 pixel kinoforms were calculated using the Gerchberg–Saxton algorithm.<sup>33</sup>

The diffractive optical elements (AODs and SLM) are placed in planes conjugate to the back aperture of the microscope objective using relay lenses. The afocal optical system comprises lenses *L*<sub>1</sub> (*f* = 20 cm), *L*<sub>2</sub> (*f* = 40 cm), *L*<sub>3</sub> (*f* = 40 cm), *L*<sub>4</sub> (*f* = 40 cm). The focal lengths of lenses *L*<sub>1</sub>, *L*<sub>2</sub>, *L*<sub>3</sub>, and *L*<sub>4</sub>, and the separation between them are chosen to ensure that deflections of the beam produce only a change in the angle of the beam entering the back aperture of the microscope objective. Typically, the cells were trapped about 5  $\mu\text{m}$  above the surface of the cover glass to minimize spherical aberrations from the media. The laser power was measured at the back aperture of the trapping objective. Laser powers are quoted as time-averaged powers based on the duty cycle (*i.e.* the number of traps) in the time-shared array.

The heterotypic microarrays shown in Fig. 2–5 were all assembled using a time-averaged optical power of ~4 mW per trap. We established that under optimum trapping conditions the maximum radiation dose for 50% viability limits the exposure of cell to about 12 minutes, restricting the assembly time and limiting the maximum size of a single array.<sup>17,34</sup>

The total cell handling time, including loading the sample into the microfluidics, stabilizing the flow in the microfluidics, trapping the heterogeneous 3D array, photopolymerization, and thorough wash of the microfluidic channel, was under 30 min, imaging starts as soon as we induce the sender bacteria.

## Image acquisition and analysis

Immediately after photopolymerization and washing the array, we began monitoring the fluorescence, extracting the intensity from the time lapse images like those shown in Fig. 3, 4, 5, and S3

using MATLAB (V7.2, MathWorks) along with the Image Processing Toolbox (V5.2, MathWorks). The images were recorded as 16-bit grayscale TIFFs using acquisition software written in LabView (V8 National Instruments). The data was read into two-dimensional numerical arrays containing the intensity values of each pixel in the image. The images were manually cropped around the area of interest to facilitate automatic cell detection. To determine the cell location automatically, these cropped images were filtered by Fourier transforming the data, then using a Gaussian bandpass filter to eliminate the low frequency background and high frequency pixelation noise. The images were then reverse transformed, and a 90% threshold value was used to mask the image. A watershed algorithm<sup>35</sup> was then used to separate the masked regions, in order to identify the different cell locations. The coordinates associated with the centers of each of these regions were recorded yielding the individual microcolony centers.

Using these centers, a  $20 \times 20$  pixel area ( $2.5 \mu\text{m} \times 2.5 \mu\text{m}$ ) was defined around the microcolony centers. The mean of the raw pixel intensity values from each of these regions was calculated and plotted, yielding the time-intensity plots as pictured in Fig. 2B, 3D and 5D. This reveals a distribution of response times associated to individuals in the cell array-information like this is usually obscured in bulk measurements of the fluorescence that cannot monitor the same cell at different times.

### Line measurement of fluorescein diffusion in a hydrogel spot

To generate spots for the diffusion measurement, a pre-polymer solution of poly(ethylene glycol) diacrylate in M9 media was prepared at 5% (w/v) concentration, with 0.2% (v/v) 2-hydroxy-2-methyl-propiofenone photoinitiator. For alignment purposes,  $1 \mu\text{m}$  fluorescent beads were added to a final concentration of  $10^8$  beads/mL. The solution was then vortexed for 15 s.

Using  $100 \mu\text{L}$  of this solution, PEGDA spots were polymerized for 3 s with 360 nm UV light in an Ibidi® Slide VI. The channel was then washed with  $300 \mu\text{L}$  of M9 media, and the resulting gel spot placed on a laser scanning confocal microscope. The gel spot was located using the fluorescent beads embedded within it. Once the gel spot was found, a 3D stack was taken for reference.

The microscope was then set to line scanning mode, scanning through the center of the hydrogel spot. Line scanning mode was used due to its high time resolution, with a scan being taken every 3 ms or so. While taking line-scanning data, a  $50 \mu\text{M}$  rhodamine solution was flowed into the channel. The fluorescence profile was recorded until the hydrogel spot reached equilibrium with its surroundings. A final 3D stack was then taken to ensure the spot remained intact. GFP expression in a receiver array is affected solely by the concentration of C6-HSL.

The resulting data for a hydrogel spot akin to those used for the bacterial microarrays is shown in Fig. S2 in the ESI.† As seen in Fig. S2(A), an initial line scan through the gel spot shows fluorescent signal only from the beads embedded in the gel. After the rhodamine is introduced, it begins diffusing into the hydrogel, causing a gradient to form transiently between the edge and the center. By plotting the concentration in the center of the hydrogel (Fig. S2(B)), a curve can be fit to the concentration with respect to time, giving a value for the diffusion coefficient of

fluorescein in this hydrogel spot. We estimate that  $D = 9 \times 10^{-7} \text{ cm}^2/\text{s}$  for rhodamine.

### Simulation of the measurement of the dynamic response of transmitters/receivers to an inductant

We fit the fluorescence data to extract parameters that described mRFP, GFP-LVA, and luxI production and degradation within a microcolony, the IPTG and C6-HSL concentration profiles within the array, *etc.*, using simulations comprised of a finite element model for convection–diffusion transport and simple mass-action kinetics for the protein production. The strength of the effect of a transcription factor,  $X$ , on the transcription rate of its target gene is described by a Hill function,  $f(x) = \beta X^n / (K^n + X^n)$ , which is derived by considering equilibrium binding of the transcription factor to the promoter site.<sup>36</sup> The Hill function is characterized by three parameters:  $K$ , the threshold concentration of inducer which indicates 50% maximum expression;  $\beta$ , the maximal expression level of the promoter that is reached asymptotically for a large concentration of active  $X$ ; and  $n \sim 2$ , which governs the stiffness of the input function.

Relying on the relationships described by eqn (1) and (2), and constraints on the coefficients obtained from simulations of independent measurements, we simulated the fluorescence observed in the arrays and extracted parameters that described mRFP1 and GFP-LVA protein production and degradation as well as the concentration profiles within the array. In order to simulate the fluorescence observed in the arrays, we first calculated the velocity profile inside the microfluidic using the COMSOL Multiphysics simulation tool. Using the chip dimensions ( $600 \mu\text{m}$  wide channel with a  $75 \mu\text{m}$  hydrogel diameter), and assuming that the M9 solution has a similar viscosity  $\eta = 1 \times 10^{-3} \text{ Pa s}$  and density  $\rho = 1 \text{ g/cm}^3$  to water, the flow was simulated assuming a no-slip condition at the channel walls and at the hydrogel surface. Next, the diffusion in the small section of the microfluidic encompassing the gel volume was simulated. The diffusion coefficient is allowed to vary for fitting, but is initially set to  $D = 2.7 \times 10^{-6} \text{ cm}^2/\text{s}$  in solution and  $9.0 \times 10^{-7} \text{ cm}^2/\text{s}$  in the hydrogel. Concentration at the upstream boundary is set to 2 mM for IPTG and 0 for C6-HSL. The downstream boundary condition allows the signal to exit by convective flow. And finally, the bacterial production of protein is computed by coupling the resulting IPTG and C6-HSL concentration to a simple mass-action kinetics model formulated according to eqn (1) and (2)  $\beta_r$  is initially set to 20 molecules/s for transmitter cells, and  $\beta_g = 10$  molecules/s for receivers.<sup>37</sup> The parameter  $\nu$  for bacterial growth is initially set to a doubling time of 2.5 h and corrected empirically. With fluorescent proteins, there is also a time-lag associated with maturation of the protein,  $\gamma$ . For mRFP1, the half-life for maturation is 12 min<sup>38</sup> and for GFP-LVA 25 min.<sup>16</sup> LuxI, the enzyme which actually produces C6-HSL, is assumed to be stoichiometric with mRFP1. The C6-HSL production rate is initially assumed to be the  $V_{\text{max}}$  for luxI of 1.1 mol(C6-HSL)/mol(luxI)/min,<sup>39</sup> but fits have shown the rate to be  $\sim 1/3$  of that value. Cell reproduction dramatically affects the rate of protein production in a given microcolony, and therefore the signal level. We controlled the reproduction rate by manipulating the concentration and flow of nutrients through the hydrogel.<sup>40,41</sup>

## Conclusion

In summary, we have studied the effect of overlayer flow and cell position on paracrine signaling in a model that mimics some of the essential features, *e.g.* diffusive transport, of a bacterial biofilm. We have shown that variations in the local concentration of the signal in a microarray can drastically affect gene expression. “Quorum sensing” gene expression is not just a simple measure of cell density, but also acts as a sensing mechanism for the environment. Since gene expression controls phenotype, signaling could produce phenotypes that depend on the flow and the location within the array. It is known that biofilms formed in a flowing environment exhibit an architecture consisting of specialized cells.<sup>23</sup> Following Redfield,<sup>8</sup> this suggests that quorum sensing may not have evolved simply for group fitness benefits, but rather for individual fitness benefits as well, allowing the bacteria to sense and respond to their environment by using soluble factors as a kind of sonar, detecting how hindered the environment is for diffusion.<sup>6,8</sup>

Our study of these aspects of quorum sensing in bacteria is only a beginning. The same methods can be used to study cell–cell interactions in eukaryotic cells, examining a variety of processes such as stem cell differentiation or cancer metastasis. By putting cells in a broader social context, but controlling their microenvironment completely, it is possible to paint an enhanced picture of cellular behavior.

## Acknowledgements

This work is supported by grants from the NSF, NIRT # 0404030 and CCF 08–29900, and the Beckman Foundation Grant. We are also grateful to R. Weiss for the donation of receiver plasmids.

## References

- B. L. Bassler and R. Losick, *Cell*, 2006, **125**, 237–246.
- T. R. de Kievit and B. H. Iglewski, *Infect. Immun.*, 2000, **68**, 4839.
- C. Fuqua and E. P. Greenberg, *Nat. Rev. Mol. Cell Biol.*, 2002, **3**, 685–695.
- W. C. Fuqua, S. C. Winans and E. P. Greenberg, *J. Bacteriol.*, 1994, **176**, 269.
- M. B. Miller and B. L. Bassler, *Annu. Rev. Microbiol.*, 2001, **55**, 165–199.
- B. A. Hense, C. Kuttler, J. Müller, M. Rothballer, A. Hartmann and J. U. Kreft, *Nat. Rev. Microbiol.*, 2007, **5**, 230–239.
- A. R. Horswill, P. Stoodley, P. S. Stewart and M. R. Parsek, *Anal. Bioanal. Chem.*, 2007, **387**, 371–380.
- R. J. Redfield, *Trends Microbiol.*, 2002, **10**, 365–370.
- M. E. Davey and G. A. O’Toole, *Microbiol. Mol. Biol. Rev.*, 2000, **64**, 847–867.
- L. Hall-Stoodley, J. W. Costerton and P. Stoodley, *Nat. Rev. Microbiol.*, 2004, **2**, 95–108.
- P. Watnick and R. Kolter, *Am. Soc. Microbiol.*, 2000, 2675–2679.
- J. S. Webb, M. Givskov and S. Kjelleberg, *Curr. Opin. Microbiol.*, 2003, **6**, 578–585.
- E. Guiot, P. Georges, A. Brun, M. P. Fontaine-Aupart, M. N. Bellon-Fontaine and R. Briandet, *Photochem. Photobiol.*, 2002, **75**, 570–578.
- K. Nilsson and K. Mosbach, *FEBS Lett.*, 1980, **118**, 145–150.
- S. Basu, Y. Gerchman, C. H. Collins, F. H. Arnold and R. Weiss, *Nature*, 2005, **434**, 1130–1134.
- J. B. Andersen, C. Sternberg, L. K. Poulsen, S. P. Bjorn, M. Givskov and S. Molin, *Appl. Environ. Microbiol.*, 1998, **64**, 2240.
- J. M. Mirsaidov, J. Scrimgeour, W. Timp, K. Beck, M. Mir, P. Matsudaira and G. Timp, *Lab Chip*, 2008, **8**(12), 2174–2181.
- J. M. Pedraza and A. van Oudenaarden, *American Association for the Advancement of Science*, 2005, pp. 1965–1969.
- J. M. Raser and E. K. O’Shea, *Science*, 2005, **309**, 2010–2013.
- E. Hiszyczynska-Sawicka and J. Kur, *Plasmid*, 1997, **38**, 174–179.
- D. De Beer, P. Stoodley, F. Roe and Z. Lewandowski, *Biotechnol. Bioeng.*, 1994, **43**, 1131–1138.
- A. B. Pratt, F. E. Weber, H. G. Schmoekel, R. Mueller and J. A. Hubbell, *Biotechnol. Bioeng.*, 2004, **86**, 27–36.
- D. G. Davies, M. R. Parsek, J. P. Pearson, B. H. Iglewski, J. W. Costerton and E. P. Greenberg, *Science*, 1998, **280**, 295.
- T. R. De Kievit, R. Gillis, S. Marx, C. Brown and B. H. Iglewski, *Appl. Environ. Microbiol.*, 2001, **67**, 1865.
- A. Kharazmi, B. Giwercman and N. Høiby, *Methods Enzymol.*, 1999, **310**, 207–215.
- K. Lewis, *Antimicrob. Agents Chemother.*, 2001, **45**, 999.
- S. L. Percival and P. G. Bowler, *WOUNDS*, 2004, **16**, 234–239.
- V. W. Serralta, C. Harrison-Balestra, A. L. Cazzaniga, S. C. Davis and P. M. Mertz, *WOUNDS*, 2001, **13**, 29–34.
- H. A. O’Connell, G. S. Kottkamp, J. L. Eppelbaum, B. A. Stubblefield, S. E. Gilbert and E. S. Gilbert, *Applied and Environmental Microbiology*, 2006, **72**, 5013–5019.
- H. Yu, C. M. Alexander and D. J. Beebe, *Lab Chip*, 2007, **7**, 726–730.
- G. H. Underhill, A. A. Chen, D. R. Albrecht and S. N. Bhatia, *Biomaterials*, 2007, **28**, 256–270.
- W. G. Koh, L. J. Itle and M. V. Pishko, *Anal. Chem.*, 2003, **75**, 5783–5789.
- V. A. Soifer, V. Kotlyar and L. Doskolovich, *Iterative methods for diffractive optical elements computation*, Taylor & Francis, London, 1997.
- U. Mirsaidov, W. Timp, K. Timp, M. Mir, P. Matsudaira and G. Timp, *Phys. Rev. E*, 2008, **78**, DOI: 10.1103/PhysRevE.78.021910.
- R. C. Gonzalez, R. E. Woods and S. L. Eddins, *Digital Image processing using MATLAB*, Pearson Prentice Hall, Upper Saddle River, NJ, 2004.
- U. Alon, *An Introduction to Systems Biology: Design Principles of Biological Circuits*, Chapman & Hall/CRC, Boca Raton, FL, 2007.
- J. Yu, J. Xiao, X. Ren, K. Lao and X. S. Xie, *American Association for the Advancement of Science*, 2006, pp. 1600–1603.
- G. Jach, M. Pesch, K. Richter, S. Frings and J. F. Uhrig, *Nat. Methods*, 2006, **3**, 597–600.
- A. L. Schaefer, D. L. Val, B. L. Hanzelka, J. E. Cronan and E. P. Greenberg, *Proceedings of the National Academy of Sciences of the United States of America*, 1996, **93**, 9505–9509.
- R. Kolter, D. A. Siegle and A. Tormo, *Annu. Rev. Microbiol.*, 1993, **47**, 855–874.
- J. Monod, *Annu. Rev. Microbiol.*, 1949, **3**, 371–394.